

Bidirectional Origami Inspiring Versatile 3D Metasurface

Ruixuan Zheng, Ruhao Pan, Chi Sun, Shuo Du, Aizi Jin, Chensheng Li, Guangzhou Geng, Changzhi Gu,* and Junjie Li*

Micro/nano origami is a fascinating 3D fabrication technology, showing a strong ability to control structural space degrees of freedom, but which are usually only able to achieve single-direction origami and hence its controlling spatial orientation is still limited to a certain extent. Here, the bidirectional origami induced by focused ion beam irradiation is proposed to break through the freedom of structural space control and realize challenging 3D micro/nanofabrication. It is found that the FIB-induced bidirectional deformation mainly relies on both materials and the ion doses, and the deformation degrees can be tuned by ion irradiated doses, which greatly contributes to construct large numbers of diverse 3D structures. Further, the underlying physics of FIB induced origami are discussed by Monte Carlo simulations along with experiments to reveal that the amounts of atoms sputtering determines the initial direction of deformation. This bidirectional origami exhibits unique capabilities in design and fabrication of versatile 3D metasurface devices. With this strategy, a 3D chiral metasurface composed of an array of bidirectional folded split ring resonators is achieved, showing a giant circular dichorism as high as 0.78/0.85 (Experiment/Simulation) in the mid-infrared region. Such powerful bidirectional origami paves high efficiency approach to broaden 3D micro/nano photonics device.

of origami methods have been realized by tensile/compressive stress of the 2D films, completing the fabrication approaches of the 3D micro-nano structures.^[7–11] Diverse form origami can be constructed from 2D patterns under different driving forces, and these methods including compression buckling,^[12,13] residual stress induced bending,^[14–16] and capillary force origami^[17,18] and electron beam induced origami^[19,20] have been developed to assemble the 3D configurations from 2D patterns. Although these methods have been used in process 3D chiral metasurface,^[21,22] SERS substrates,^[19] devices,^[23–25] which are face with problems in the controllability, such as the limitation of available materials, single origami direction, fine control in 3D micro/nanoscale.

As is well known, focused ion beam (FIB) technology has huge advantages in micro/nano fabrication,^[26–30] such as the energy and dose of ion beam can be controlled continuously, the morphological changes of the samples can be observed in situ and its high machining

accuracy reaches nano size.^[31] Thus, FIB can be used for the manufacturing of configurations with material versatility, abundant spatial orientation, and high fabrication accuracy.^[32,33] Most importantly, 3D micro/nano origami can be achieved easily by FIB irradiation inducing deformation (folding or bending). However, the existing folding and bending structures have a single deformation direction, which remains subject to significant restrictions in dexterity. In other words, these methods do not exploit the enigmatic potential of FIB processing that have not reached the fabrication with bidirectional deformation. On the one hand, the achievements are still incomplete and not profound, especially in the terms of alternative materials,^[34] flexible folding/bending directions and its behind physics mechanism. On the other hand, the 3D origami devices have been an emerging field for researchers to focus on, and it is great significance for practical applications and achieving higher efficiency. Therefore, further investigates are bound to dig the processing potentials of FIB induced micro/nano origami for broad application in expansive fields. The freedom of structural space control is challenging for 3D micro/nanofabrication, but which is very important for micro/nano photonics, and also open up more possibilities for multi-dimensional light field regulation. For example, the inherent spin selection characteristics of chiral structures greatly depend on the spatial configuration of the stereo, but the existing fabricating


1. Introduction

Origami, the ancient art of paper allows the transformation of flat sheets into macroscale 3D folding/bending structures, is always fascinating due to its unique combination of outstanding properties including reconfigurability, loading ability, folding ability, bending ability, and twistable capability, which greatly enriches the diversity of 3D configurations.^[1–6] Up to now, series

R. Zheng, R. Pan, C. Sun, S. Du, A. Jin, C. Li, G. Geng, C. Gu, J. Li
Beijing National Laboratory for Condensed Matter Physics
Institute of Physics
Chinese Academy of Sciences
Beijing 100190, P. R. China
E-mail: czgu@iphy.ac.cn; jjli@iphy.ac.cn

R. Zheng, C. Sun, C. Li, G. Geng, C. Gu, J. Li
School of Physical Sciences
CAS Key Laboratory of Vacuum Physics
University of Chinese Academy of Sciences
Beijing 100049, P. R. China

J. Li
Songshan Lake Materials Laboratory Dongguan Guangdong
Guangdong 523808, P. R. China

 The ORCID identification number(s) for the author(s) of this article can be found under <https://doi.org/10.1002/admt.202200373>.

DOI: 10.1002/admt.202200373

methods are difficult to provide higher degrees of freedom. FIB induced micro/nano origami is expected to contribute more to the freedom of structural space control.

In this work, an FIB-induced bidirectional origami method is proposed, which can break through the freedom of structural space control and realize challenging 3D micro/nanofabrication and achieve controllable bending/folding directions of different materials. We discover that the initial direction of origami varies with the materials. For the monolayer 50 nm SiN_x film, the deformation deviating from the incident direction of ion beam is realized by FIB. Then, the bilayer films are prepared by physical deposition, which not only realized upward deformation, which indicates the deformation toward to the ion source, of Au film, but also achieved bidirectional origami for numbers of materials, such as Al, Ti, and Al₂O₃. The behind physics of the bidirectional origami are further discussed by the results of both Monte Carlo simulations and experiments, indicating the stresses are mainly caused by the vacancies. Particularly, the key factor in the direction of deformation is atomic sputtering quantity, which can be proved by the surface characterization, for instance the grain sizes change and the surface roughness of the materials during the irradiation. Importantly, based on above FIB origami strategy, a 3D chiral metasurface with bidirectional folded split ring resonators (SRRs) are designed and constructed, which shows a giant circular dichroism (CD) as high as 0.78/0.85 (experiment/simulation) in the mid-infrared region. Our work broadens greatly the fabrication capacity of FIB-induced origami and lay a new foundation for the design and realization of 3D multifunctional micro/nano photonic devices in the future.

2. Results and Discussions

2.1. FIB-Induced Bidirectional Origami

The fabrication process of 3D origami induced by FIB is depicted in **Figure 1**, mainly including four steps from 2D films to the 3D structures. First of all, suspended SiN_x film on the Si window is prepared. The suspended thin SiN_x substrate plays a good role in patterning and carrying other materials without affecting the effect of origami processing. Then, the photoresist is spin coated on the samples and patterned by electron beam lithography (EBL). The SiN_x films with patterns are obtained after the dry etching program. Next, the other materials can be deposited on the films to form bilayer cantilevers by electron beam deposition or atomic layer deposition. This step can be eliminated if the monolayer SiN_x film will be fabricated, as shown in Figure S1a, Supporting Information. Finally, these double cantilevers can be transformed into 3D origami induced by FIB irradiation. The folded structures are realized by line scanning, while the bended structures correspond to global method. Importantly, the direction of origami can be changed by increasing the ion doses for some materials. Origami deforms away from the direction of the ion beam incidence for low ion doses, which is defined as downward. Further, the origami deforms toward the direction of the ion beam incidence with ion dose increasing, which is called upward. So, the ion scanning mode determines the folding or bending deformation, while the amount of ion dose controls origami direction as

so to realize the bidirectional origami. What is more, in order to facilitate the expression of the relationship between the origami deformation amplitude and the ion beam dose that the folding angle α and crimped curvature $\theta = \beta/l$ are defined in inset of Figure 1a, where the minus sign means down below the frame and vice versa. The deformation from bottom to top can be observed in Movie S1, Supporting Information. This bidirectional origami technique will greatly satisfy the multi-degrees of freedom for highly sophisticated designs that provide the possibility of realizing new device applications. As shown in Figure 1d, the folding can be bidirectional and programmable for materials by parameters of FIB.

For the purpose of investigating the deformation of SiN_x films under FIB irradiation, SiN_x cantilevers with a length of 3 μm are fabricated, whose widths is ranged from 0.5 to 4 μm . The FIB line and area scanning with different ion doses are applied to the cantilevers, respectively, which introduces a stress on the 2D patterns and the certain bending/folding angles are obtained. It is found that a single layer SiN_x film only produces a downward direction of origami (folding and bending) despite increasing the ion doses (Figure S1, Supporting Information). To satisfied numerous applications of origami technology, variable bilayer films can be introduced to be converted to 3D origami by FIB, and the relationships between origami features and processing conditions should be established. Metals with peculiarity of corrosion resistant and ductile are good choices for FIB induced origami. Here, the bilayer films composed of 20 nm SiN_x and 80 nm Au or Al are selected, and their cantilevers with different widths and lengths have favorable consistency in the fabrication. From the **Figure 2a**, the folded Au/SiN_x and Al/SiN_x with different widths verify that the folding angle can be flexibly controlled by changing the doses of the line scanning. However, Au/SiN_x have a monotonous upward deformation, whereas Al/SiN_x can deform downward at first and then upward with irradiation doses. In the interests of two distinct deformations, the relationships between folding angle α and ion dose are summarized in Figure 2b for three kinds of materials. It can be clearly seen that the downward folding increases with the continuously irradiation of FIB, as exhibited a minimum folding angle of -68° can be reached for the ion dose of 14.7×10^{11} ions cm^{-1} for single layer SiN_x (blue line). The Au/SiN_x bilayers can be folded upward and reach a maximum angle of 90° at about 16.2×10^{11} ions cm^{-1} (gold line). While the Al/SiN_x films will be folded downward to bottom angle of -46.3° at 6.2×10^{11} ions cm^{-1} , then the upward folding trend can be observed with the continuous increase of dose and they finally stand vertical at 64.8×10^{11} ions cm^{-1} (black line). The thickness of SiN_x film will have a certain effect on origami, and a larger thickness will be induced a smaller deformation for the same dose.

In addition, Figure 2c depicts two arrays of homogeneous bended Au/SiN_x and Al/SiN_x films, respectively. Similar to the situation in the line scan, the bilayers are bent into different directions in the initial period. And uniformity states can be achieved for the same ion dose regardless of the length of the cantilevers, while the independence of the curvature to the ion dose are summarized in Figure 2d. The SiN_x patterns can reach a maximum deformation of approximately $-0.07 \mu\text{m}^{-1}$ at 7.8×10^{14} ions cm^{-2} doses (blue line) with only downward deformation. And for Au bilayer bended upward

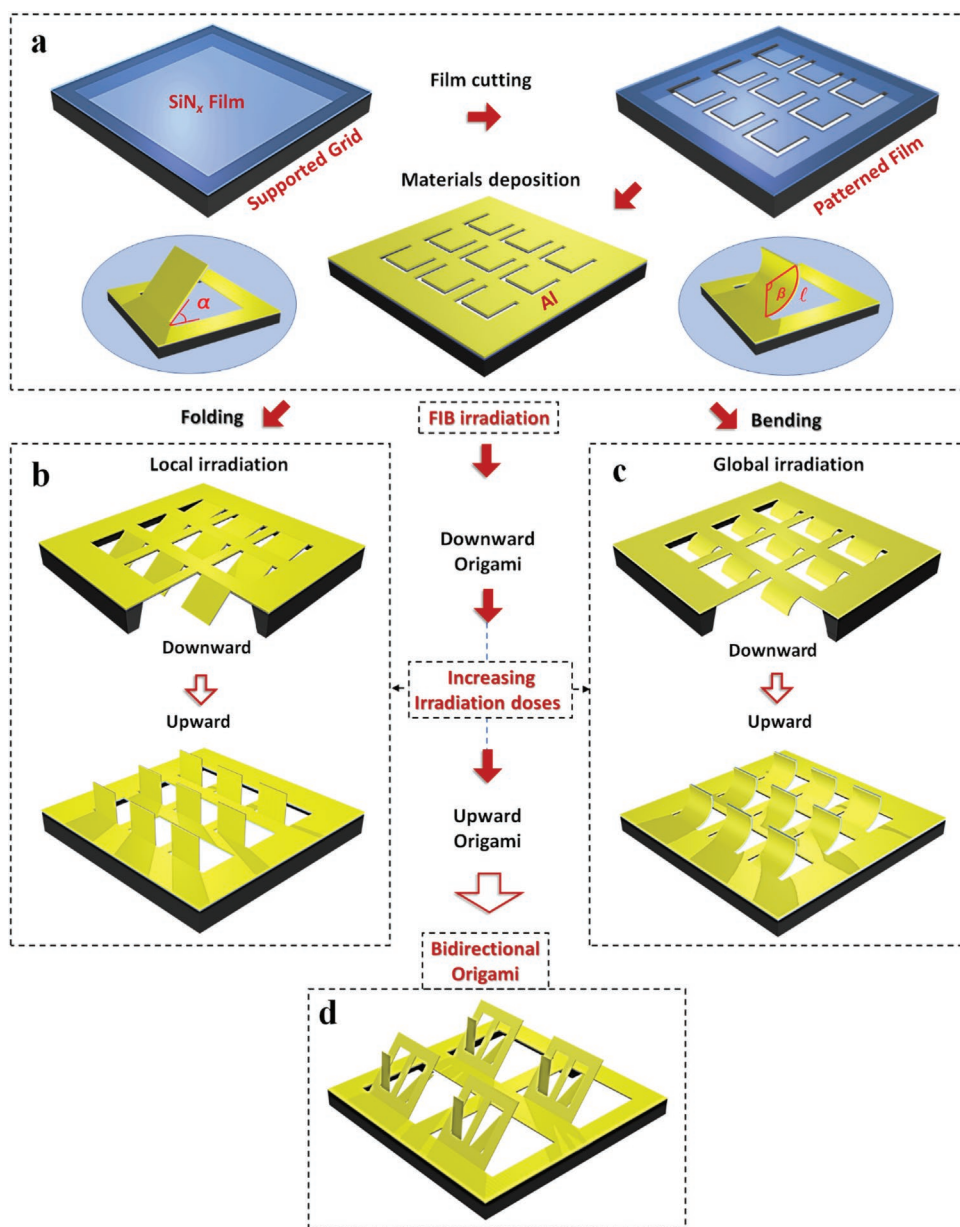


Figure 1. Schematic of the processes to fabricate 3D bidirectional origami structures. a) Preparing first the suspended SiN_x film on the Si window, and next 2D patterned films are acquired by EBL and RIE etching, and then metal or metal oxide are deposited on the single layer SiN_x films. The insets show the expression of the degree of deformation. Where α is folding angle, β is central angle, and l is arc length. b) 3D folding double layers structures by FIB line scanning. c) 3D bending double layers structures by FIB global scanning. d) Bidirectional origami combined the downward and upward deformation.

under global scanning, they reach the maximum curvature is about $0.34 \mu\text{m}^{-1}$ at $74 \times 10^{14} \text{ ions cm}^{-2}$ (gold line). Meanwhile, the Al is bend downward to about $-0.13 \mu\text{m}^{-1}$ curvature at $8.0 \times 10^{14} \text{ ions cm}^{-2}$. Following, they begin to bending upward until attain the maximum curvature of about $0.47 \mu\text{m}^{-1}$ at $146.3 \times 10^{14} \text{ ions cm}^{-2}$ (black line). Above results indicate FIB induced origami depends on both the materials and ion doses, but an inflection point from downward to upward origami only occurs in the Al/SiN_x . Figure 2e shows flower-shaped 3D structure based on the deformation effect of different materials. The unidirectional and bidirectional origami characteristic

is reflected in the SiN_x (downward) or Au/SiN_x (upward) and Al/SiN_x (both downward and upward) in sequence, which verify directly the feasibility of bidirectional deformation by FIB irradiating Al/SiN_x . Obviously, only the choice of Al/SiN_x for fabrication can better reflect the freedom of processing and maximize the advantages of bidirectional origami. In addition, the size has no obvious influence on the origami effect from our processing of the cantilevers with different aspect ratio. However, the thickness of the SiN_x affects the final deformation curvature in the case of film bending,^[3] because the maximum stress of a metal film that FIB can introduce is limited.

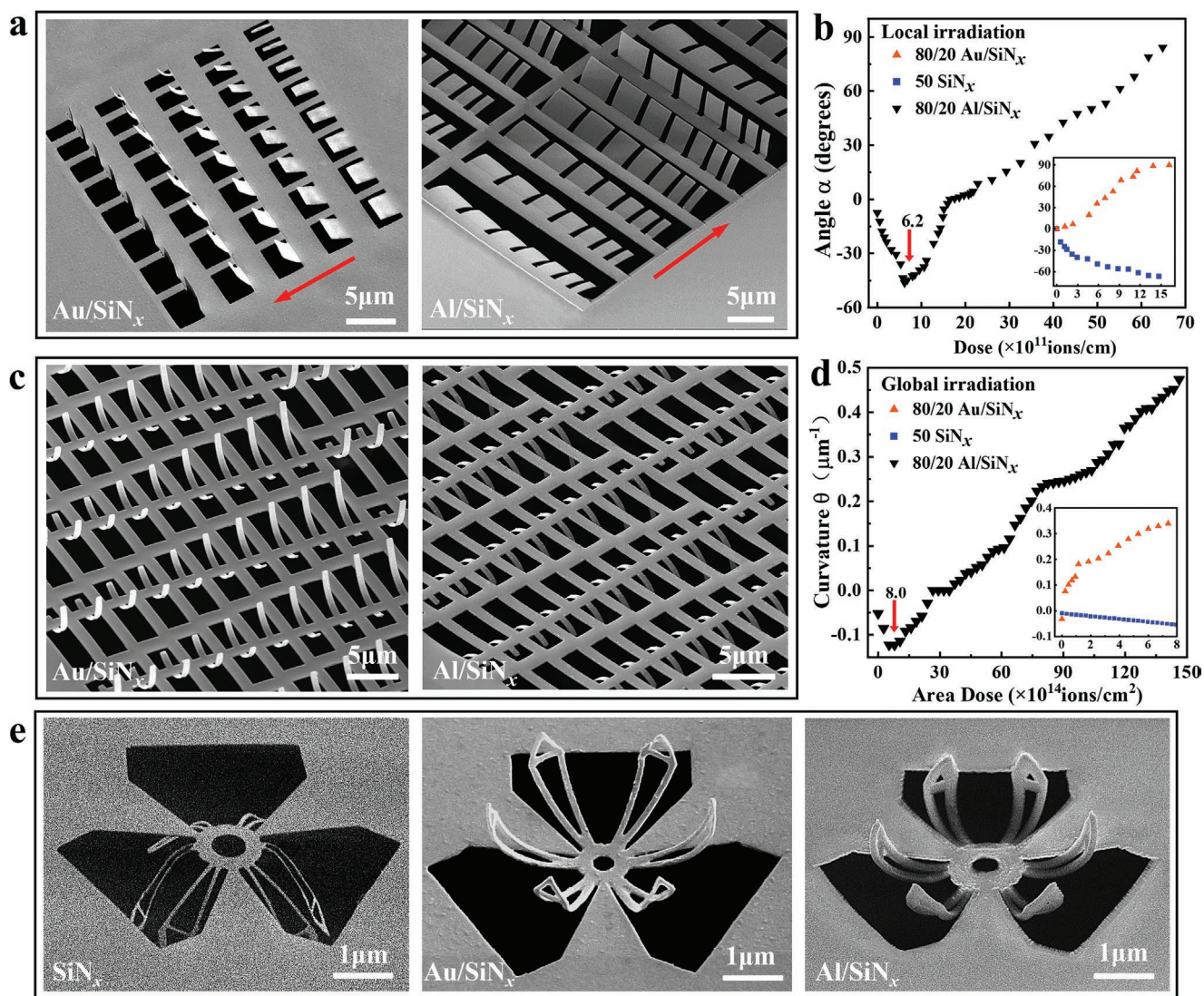


Figure 2. The SEM images of origami for 80/20 nm Au/SiN_x and Al/SiN_x in 52° tilted view and the relationships between the ion doses and certain angles or curvatures. a) SEM images of different angles of folded cantilevers with different widths, where the red arrow indicates the direction of the dose increase. b) The relationships between the ion line doses and fold angles. c) SEM images of different curvatures for bended cantilevers with changed length. d) The relationships between the ion area doses and curvatures. e) SEM images for three different 3D morphologies of bended flowers for 50 nm SiN_x, 80/20 nm Au/SiN_x, and Al/SiN_x (from left to right).

It is not hard to think that the bidirectional deformation can be continuously controlled over a large scale, thus the origami with ample morphology can be fabricated. Thanks to the bidirectional controllability of the FIB, abundant configurations based on Al/SiN_x that combine the bending and folding modes are fabricated, as shown in Figure 3. First, precise area scanning can control the bending of individual structures (the wing) from downward to upward for complex butterfly patterns, as shown in Figure 3a. Second, the folded petals are processed by irradiating the surface and line scanning the local parts, demonstrating flexible and optional processing capabilities in Figure 3b. Similarly, in Figure 3c, to manufacture this form combining bending and folding, the curved structure is obtained and then folded with followed by surface irradiation by sequency. The nested bidirectional origami structure in

Figure 3d displays the amazing fabrication capability, which show the possibility to fabricate 3D structures with both bidirectional folded and bended parts for higher efficiency even novel functions. In other words, the functions of the micro/nano origami could be axially customizable throughout the patterning parameters. Meanwhile, this repeatable structural machining validates the overall approach as well as the effectiveness of bidirectional fabrication process, especially for Al.

2.2. Analysis and Verification of Principle

For better understanding of the phenomena of FIB-induced stress, the behind physics reasons of the origami are further investigated with the aid of Monte Carlo simulation by

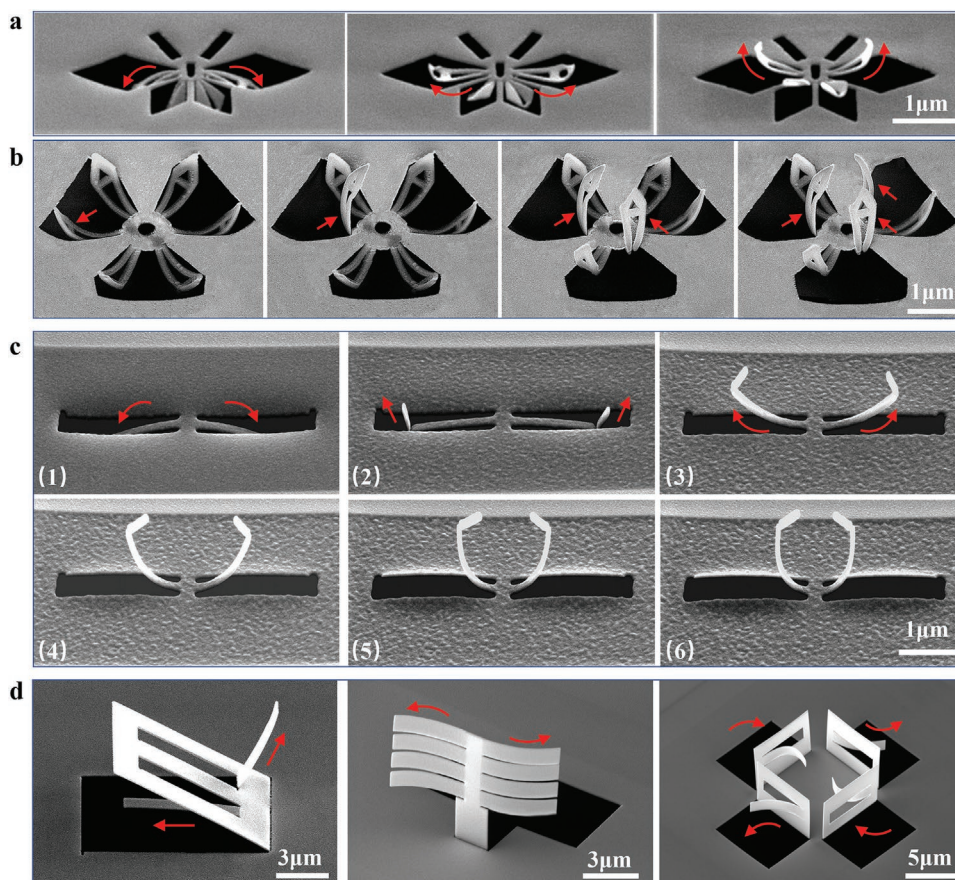


Figure 3. SEM images of complex origami with folding or/and bending. a) A bending wing of the butterfly is transformed downward to upward by global incidence. b) Fold selected curved petals. c) A cantilever fabricated combining bending and folding with varying degrees of deformation. d) Bidirectional origami construct various folding/bending complex structures. Red arrows in the SEM images highlight the different directions of origami deformation.

“Stopping and Range of Ions in Matter” (SRIM) software,^[32] which can imitate the process of ion beam implantation in targets. It is a clever approach to track the positions of particles, recoil atoms and secondary particles. The energy parameters of each atom are listed in Figure S2a, Supporting Information, which affects the impact of atomic interactions between ions and the target. The paths and damage extents of 50 nm SiN_x, 80 nm Au, and 80 nm Al affected by ion implantation are displayed in Figure S2b,c, Supporting Information, in sequence. These figures not only show the damage range caused by ion beam implantation, but they also display the relationships between ion beam energy and injection depth and vacancy production. The damage effects caused by ion beam implantation present a Gaussian distribution, and the statistical data is set as the expected value.

By summarizing and analyzing the simulations, the physical reasons of FIB-induced origami can be better understood. The dependences of projection injection range and vacancies/ion on variable voltages are enumerated in Figure 4a. It is apparent that the number of vacancies produced has increased due to the increase of ion energy. Simultaneously, the damage ranges have increased significantly as well. Although Al can be damaged more extensively at the same energy, the surface of gold can produce a richer number of vacancies. Furthermore, the sputtering amount of Au (4.1) is much larger than that of Al

(0.81), as shown in the graph of the sputtering amounts per ion caused by the initial contact of ions with materials (Figure 4b). Thus, it can be inferred that the ion impact contributes to the mass of atoms escaping from the gold surface and causing vacancy defects. In contrast, the wide distribution of vacancies in aluminum is due to implantation defects caused by ion collisions, which indicates that the grain boundary of the surface material increases and the volume expands. Therefore, the key factor determining the direction of origami is determined as the unit sputter amount, and downward deformation occurs when the value is less than 1. However, as the materials continue to be etching, their surface binding energy decrease and the sputtering amounts begin to rise. Thereupon, there will be a gradual upward deformation trend. In addition, the concentrated damage range leads to a faster deformation rate, which means much steeper deformation curve with the dose. The change of sputtering amount with incident angle is also worth paying attention to, so the relationship between Al sputtering amount and incident angle is established in the insert of Figure 4c. The experiment likewise demonstrates that the amount of sputtering can be adjusted by changing the ion incidence angle and the deformation direction can be controlled. The great match between simulation analysis and experimental phenomena confirms the universality of our interpretation of FIB-induced deformation (Figure S3, Supporting Information).

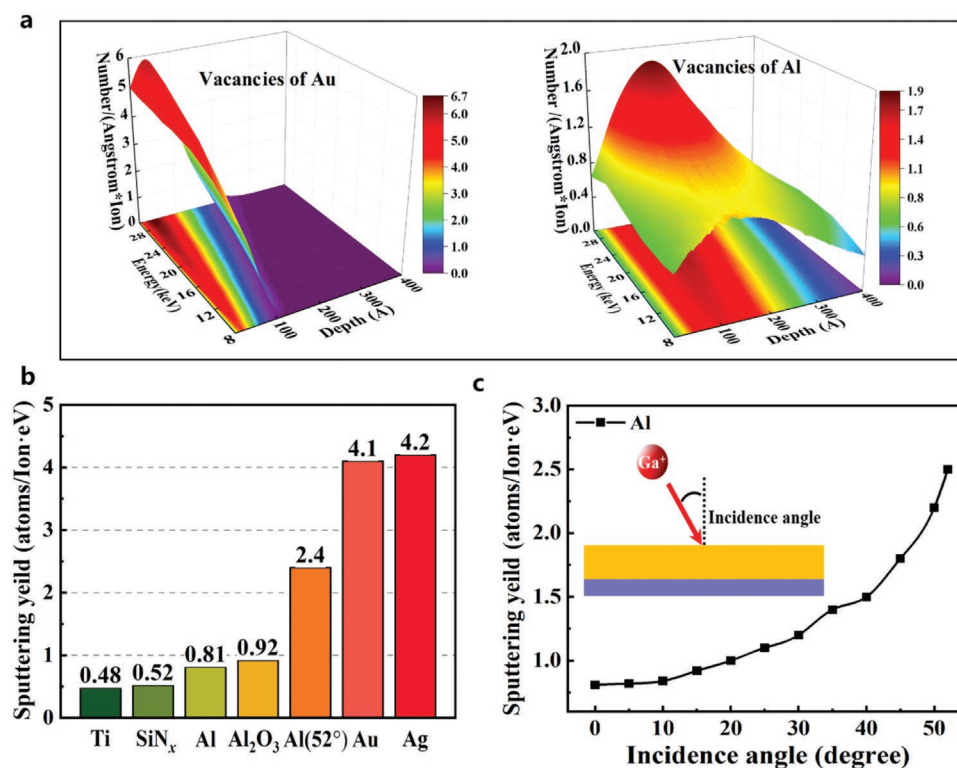


Figure 4. Monte Carlo simulation data summary. a) The relationship between the number of vacancies generation and ion energy for 80 nm Au (left) and Al (right). b) Atom sputtering amounts of different materials in this work. c) The dependence of sputtering yield on the injection angle with an inset schematic.

The more intuitive microscopic process of bidirectional origami is presented in **Figure 5a**, and the induced stress produced can be divided into two models. When the amount of sputtering is low, the ion implanted material causes surface volume expansion and induces downward deformation of extrusion stress. On the contrary, when the amount of sputtering is large, FIB etches the surface material and causes atomic loss, resulting in surface tensile stress and upward origami. Fortunately, the characterizations of irradiated materials support our interpretation. As an example, the **Figure 5b** shows the SEM images of the surface differences of the target material Al under different dose irradiations. Distinct difference between the downward and upward origami can be observed. At the initial stage of ion beam incidence, the surface of target Al remains smooth. However, the surface is obviously roughened by etching when the deformation direction is upward. Moreover, the AFM measurements provide more evidences for our interpretation, and the variation trend in **Figure 5c** is consistent with that in **Figure 2d**. The Al surface roughness is refined about from 1.5 to 1.1 nm at 7.1×10^{14} ions cm^{-2} , and the corresponding grain size is approximately reduced from 58 to 53 nm under at beginning. Subsequently, the sizes grow up to about 73 nm and roughness reached 2 nm with grains aggregate, which results in grain boundary fusion and the density increase. The corresponding SEM insets of surface can clearly give evidence of the variation trend of the grain sizes. The change of surface grains morphology under ion injection is the primary source to induce stress and realize origami. This helpfully establishes a new understanding of the relationship between grain and stress and strain of micro/nano material.

2.3. Bidirectional Origami Chiral Metasurface

Bidirectional origami not only enables a clearer and more accurate understanding of ion beam induced stress, but also makes it possible to process more dimensional structures and provide more space choices for constructing various 3D constructions in micro/nanoscale, especially for 3D metasurface with excellent performances relied on spatial complexity. For this propose, a metasurface consist of bidirectional folded SRRs has been designed and fabricated by FIB-induced origami. The two cantilevers of the SRR are folded bidirectionally, delivering surprising chiral optical selectivity in the mid-infrared band (4–16 μm). Naturally, the circular dichroism (CD) spectra ($\text{CD} = |T_{\text{LCP}}| - |T_{\text{RCP}}|$) is calculated to testify the chirality of this chiral metasurface, where T_{LCP} and T_{RCP} are the transmission of the left circularly polarized (LCP) and right circle polarized (RCP) incident light, severally.

In order to get the optimal spin states selection ability, finite-difference time-domain (FDTD) method is used to optimize the structural configuration of the SRR. By elaborately designing the geometrical parameters of the folded SRR, which accommodates the resonance of both responses is identified. The feature sizes that labeled in the inset of **Figure 6a** are $p = 4 \mu\text{m}$, $l = 3.6 \mu\text{m}$, $w = 2 \mu\text{m}$ and $d = 0.65 \mu\text{m}$. Each unit consists of 20 nm SiN_x support frame and a 70 nm Al SRR with folding angles $\varphi/-\varphi'$. **Figure 6b** shows the change of CD values with the variation of same upward and downward folding angles, which determines the intrinsic chirality of the structures. It can be obviously seen that the extremal of the CD values is appear

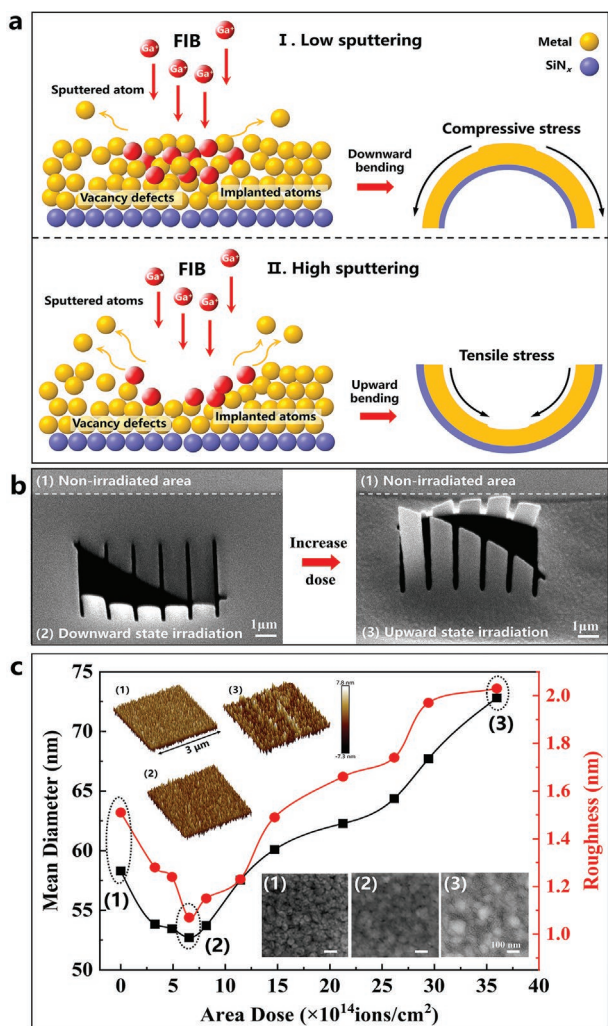


Figure 5. Principle characterization of FIB induced stress and experimental verification. a) The physical models of the stress induced by ion beams with lower and high sputtering, in which the compressive stress and tensile stress is responsible for upward and downward origami, respectively. b) SEM images of bended Al/SiN_x film induced by different doses at globe irradiation mode, where the area of (1), (2), and (3) mark the surface area morphologies for non-irradiation, downward state, and upward state irradiation, respectively. c) Measurements of the mean grain sizes and surface roughness of Al/SiN_x film for different area doses, where the illustrations are the SEMs and AFM images of the area of (1), (2), and (3), respectively.

both at 5.12 and 11.33 μm for the SRRs with both inverse 45° folding angle, which means the intrinsic chirality of this structure affects its intense interaction with circularly polarized (CP) light. Figure 6c further reveals that CD transforms with folding angle of a single arm, while the other arm of the SRR maintain a folding angle of -45° . And $\varphi = \varphi' = 45^\circ$ is also verified to be the most suitable folding angle for this resonator. Thanks to this configuration, the simulated transmission spectra under the incidence of LCP (red circle) and RCP (blue circle) are presented in Figure 6d, bring out that high CD values of 0.85 at 5.12 μm and -0.86 at 11.33 μm , respectively.

Based on bidirectional technology, this metasurface has been accurately fabricated that the planar SRRs in Figure 7a deforms

into 3D chiral structures. It is clear that large areas of periodic elements are prepared, and the 45° folding angle could be better observed in the enlarged inset of Figure 7b. Focusing on the positive CD value, the chiral metasurface is spectroscopically examined for resonance responses at short wavelengths. The corresponding experimentally measured transmission properties for LCP and RCP incidence are shown in Figure 7c. A large CD up to 0.78 is experimentally achieved at the 5.13 μm for this metasurface, and the transmittance of the LCP and RCP light can be reversed by changing the orientation of the folded SRRs. It is evident that the simulation results agree well with the measured data, where the slight difference in resonant strength primarily arises from the size mismatch and imperfections in the fabrication process. And plasma resonance mode on the surface of SRR is affected by the dielectric material losses from the thin surface oxidized of Al. Meanwhile, the inevitable signal noise in spectral measurement also affects the functional efficiency. To elucidate the underlying physics of the spin resolved characteristics that observed in the bidirectional folded metasurface, the radiated powers of multipole moments and surface current distributions induced under excitation with LCP and RCP light are quantitatively analyzed.

Figure 7d shows the dispersion of radiation power for multipole moments, which calculated from the induced currents in the folded SRR with LCP and RCP incident waves, respectively. Obviously, the radiations of the metasurface under illumination of circular polarized light with distinct spin states are significantly different. The total scattering efficiencies for the folded SRR with RCP incident light are more than 1 order of magnitude higher than that of with LCP one, which agrees well with the transmission spectra. As shown in Figure S4a, Supporting Information, the magnitude intensity of the electric dipole moment for RCP incidence is about 17.5 times more than that for LCP one, and the magnitude of the magnetic dipole moment is about 22 times. What is more, the intensity of toroidal dipole is also about 15 times stronger for RCP incidence at 58.6 THz than LCP mode. Contrary to the components of multipoles for LCP incident light, the components of P_y , P_z , M_x , M_y , and T_y over than LCP one exhibit more powerful radiated power at the resonance frequency. What is more, the insets of Figure 7d successively depict the surface current distributions on the folded SRR at the resonant frequency for LCP and RCP incident light. The current caused by LCP incidence is negligibly weak, and the excitation modes generated by each part cancel each other. Thus, the LCP wave can propagate through the sample with high transmittance. An RCP incident wave induces strong current on the antisymmetric SRRs, which means that the RCP incident wave interacts strongly with the folded metasurface. Benefiting from surface current distributions in the folded SRR, discriminative responses in absorption and scattering to different spins of CP result in the outstanding dichroism. Analogical, a similar bidirectional bending SRR is considered, but the simulations showed that the CD value produced by bending was not better than folding, as shown in Figure S4c, Supporting Information. The corresponding multipoles scattering modes are calculated, and it is clear from the Figure S4d, Supporting Information, that the CP excitation of the two spins cannot provide strong chiral optical responses and spin selective transmission.

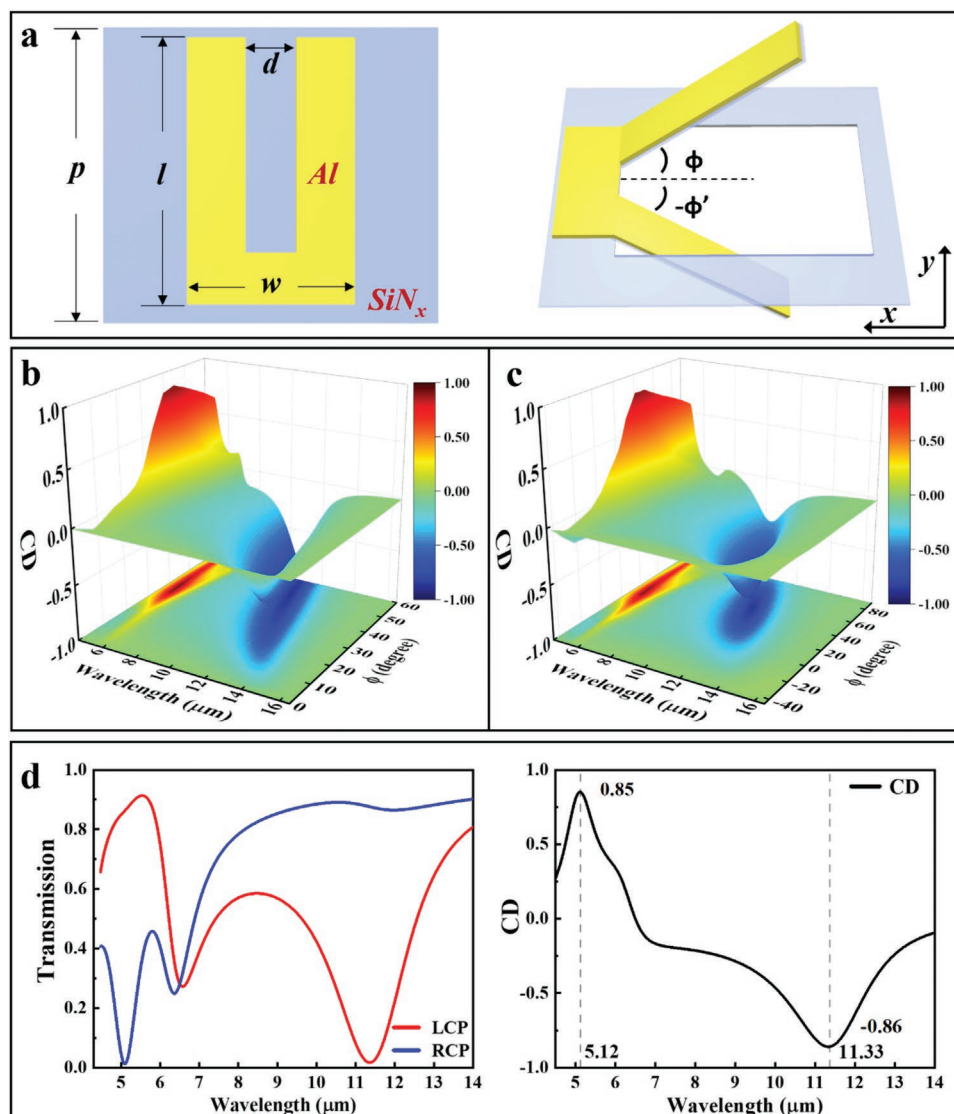


Figure 6. Simulation results and schematic diagrams of chiral structures. a) The schematic diagram of chiral structures. b) The CD values change with the variation of same upward and downward folding angle. c) The change of CD values caused by another folding angle varying when fixed the downward folding angle is -45° . d) Simulated transmission with LCP/RCP incident and CD spectra of chiral structures, respectively.

3. Conclusion

In this work, the stress induced by FIB irradiation is applied to achieve micro/nano scale origami structures, which has broken through the dimension limitation of processing arts and enriched the material selectivity. The dependences between the deformation of some film materials and line/area FIB irradiation dose are established. Especially Al/SiN_x films show a bidirectional origami property, its deformation direction goes from down to up at a key inflection point of ion dose with the increase of the ion dose. Monte Carlo simulations are used to uncover its behind physics, and the vacancy defects caused by incident ion are the main source of the stress through analysis, which leads to the transformations of both local volume and grain boundary. The simulation results reveal that a key indicator to determine the direction of origami is whether the initial sputter amount per ion is bigger than 1, where a high

sputtering rate results in the upward origami, while the low one refers to the downward origami. The variations in grain sizes and surface roughness changes of materials have been verified by AFM measurements, which is a hard evidence to judge the stress change. Impotently as-proposed bidirectional origami can enrich greatly the design of 3D metasurface, and further a chiral metasurface consisted of bidirectional 45° folded 3D SRRs is fabricated smoothly. A giant CD as high as 0.85/0.78 is obtained in the simulation/measurement, which not only reflects perfect design of 3D chiral metasurface but also means that spin-states dependent transmission is achieved in a high efficiency. The multipole expansion of the resonance uncovers that the giant CD comes from concrete scattering. Our works are conducive to better understand the stress defined by ion-matter interaction, and will strengthen the existing database of materials used for origami. Our proposed bidirectional origami arts will greatly exploit the manufacturing potential of

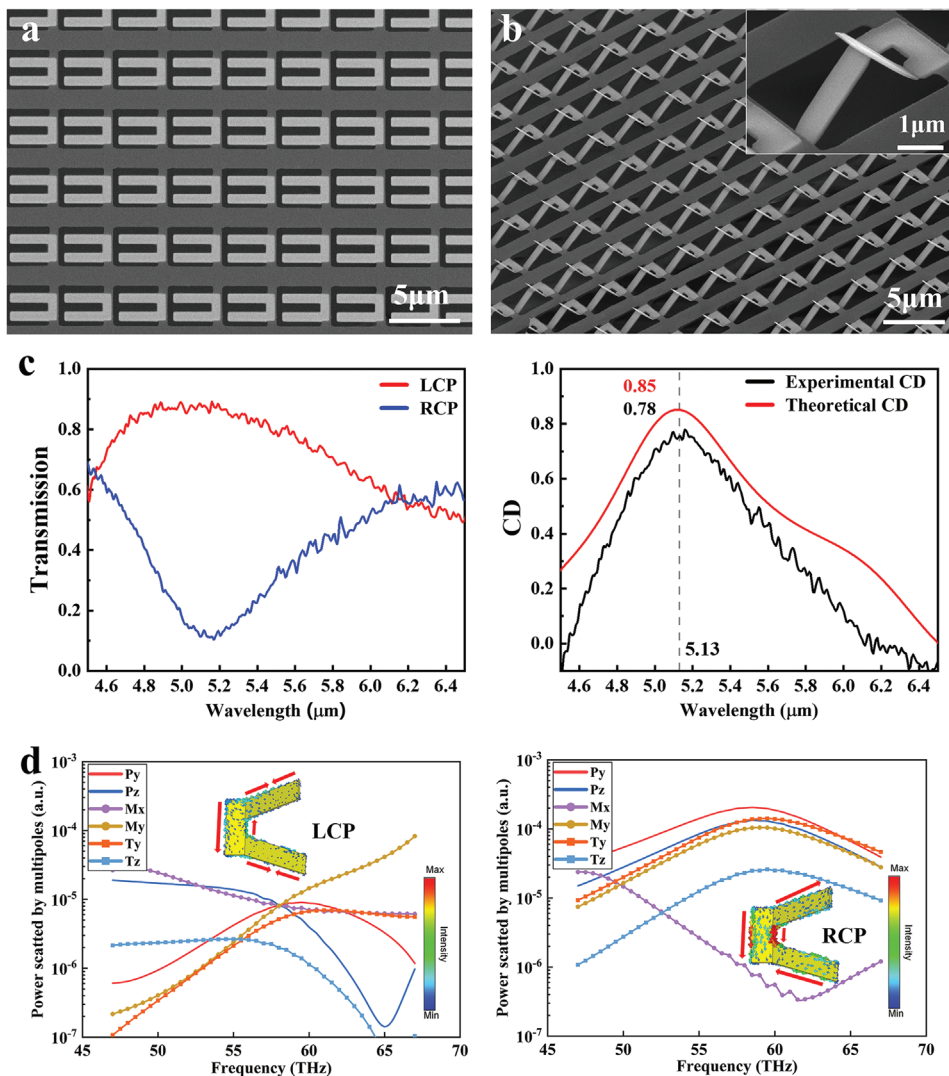


Figure 7. The experiments with SEM images and spectra, and radiation power for multipole moments. The SEM images of chiral structures for a) unfolded and b) folded SRR. c) Measured transmission with LCP/RCP incident (left) and CD spectra of metasurface with a comparison between the experiment and simulation (right). d) The radiation power for multipole moments for LCP/RCP incident, where the inset shows surface current distribution.

3D micro/nano structures and is expected to establish a robust fabrication platform in the broader fields including micro/nano-photonics, optoelectronic, and mechanical devices, etc.

4. Experimental Section

2D Pattern Preparation: The processing flow started from cleaning the $100 \mu\text{m} \times 100 \mu\text{m}$ 20 or 50 nm SiN_x film window (Ilabilab Company) with oxygen (O_2) plasma for 10 s, where the pressure was maintained at 100 mTorr with 100 sccm O_2 flow. Second, the 200 nm thick photoresist (PMMA 495 A5) was spin-coated on the dielectric films window and pre-baked at 180°C for 60 s. Then the electron beam lithography system (Raith 150) was applied to write the designed patterns. After developing in MIBK/IPA = 1:3 for 40 s, the single-layer dielectric patterns were obtained by the reactive ion etching (RIE, Plasma Pro NGP80) etching of the exposed SiN_x films and the photoresist was removed. In the etching process, trifluoromethane (CF_3) and O_2 gases were flown into the chamber, and this process was conducted at 200 W to etch SiN_x .

Next, the other materials could also be deposited on the patterns to form double-layer films by electron beam deposition (EBD, FU-12PEB) at 1 \AA s^{-1} or atomic layer deposition (ALD, Savannah-100).

FIB Origami: The patterned films were placed into the chamber of an FIB/FEB system (Helios 600, FEI) with Ga ion source. The 2D planar patterns could be folded or bended to 3D structures by the ion irradiation process with line scanning or area scanning mode. Different ion energies (8–30 KeV) and ion beam current densities (ranged from 7 pA to 65 nA) could be optionally applied to build up various 3D structures. Meanwhile, the angle between the incident direction of ion beam and the sample surface could be set in the range of -10° to 60° . The morphology of the 3D configurations prepared could be directly captured by in situ SEM images via FEB.

Monte Carlo Simulation: The collision between the implanted ion and the target atom adopted the two-body collision approximation. The random jump of the ion between the two collisions was determined by the average free path. The shielding Coulomb potential was used for the interaction potential energy between ions and atoms. The charge state of ions in solid was approximated by effective charge. The amorphous films deposited by electron beam evaporation were in line with the conditions

of amorphous target set in the software. The simulation mode was set as detailed calculation with full damage cascades and the number of ions calculated each time to be 5000 to ensure sufficient accuracy.

Numerical Simulations: In order to determine the optimal structure and clarify the mechanism of the intrinsic chiral optical responses, the metasurfaces were theoretically analyzed based on finite element method. The full wave simulations (transmission spectra and surface current distributions) were conducted with unit-cell boundary conditions in the x - y plane and Floquet ports in the z -direction for terminating the domain.

Measurements: The average grain sizes and roughness of Al film surface were measured by AFM (Dimension Edge, SPA-400) scanning with tapping mode. The Fourier-transform infrared spectrum (FT-IR) system (Bruke Vetex V80) was used to measure the transmission/reflectance spectrum of the metasurface. A sample with $100 \times 100 \mu\text{m}^2$ area was displaced under the microscope (Bruker Hyperion) with $15\times$ objective lens. The background signal was obtained from air for 128 times scanning, and then the spectrum of the chiral metasurface was obtained after 128 times scanning.

Supporting Information

Supporting Information is available from the Wiley Online Library or from the author.

Acknowledgements

This work was supported by the National Natural Science Foundation of China under Grant Nos. 12074420, U21A20140, 61888102, and 61905274, the Beijing Municipal Science & Technology Commission, Administrative Commission of Zhongguancun Science Park under Grant No. Z211100004821009, the Strategic Priority Research Program of Chinese Academy of Sciences (CAS) under Grant Nos. XDB33000000 and XDB28000000, the Key Research Program of Frontier Sciences of CAS under Grant Nos. QYZDJ-SSWSLH042 and XDPB22, and the Project for Young Scientists in Basic Research of CAS under Grant No. YSBR021. This work is also supported by the Synergic Extreme Condition User Facility, China.

Conflict of Interest

The authors declare no conflict of interest.

Data Availability Statement

The data that support the findings of this study are available from the corresponding author upon reasonable request.

Keywords

3D micro/nano-structures, chiral metasurface, FIB-induced origami, FIB-matter interaction, Monte Carlo simulation

Received: March 9, 2022

Revised: April 7, 2022

Published online:

- [1] Z. Liu, Z. Liu, J. Li, W. Li, J. Li, C. Gu, Z. Y. Li, *Sci. Rep.* **2016**, *6*, 27817.
[2] Z. Liu, S. Du, A. Cui, Z. Li, Y. Fan, S. Chen, W. Li, J. Li, C. Gu, *Adv. Mater.* **2017**, *29*, 1606298.

- [3] R. Pan, Z. Li, Z. Liu, W. Zhu, L. Zhu, Y. Li, S. Chen, C. Gu, J. Li, *Laser Photonics Rev.* **2019**, *14*, 1900179.
[4] F. Feng, P. Plucinsky, R. D. James, *Phys. Rev. E* **2020**, *101*, 033002.
[5] S. Chen, J. Chen, X. Zhang, Z. Y. Li, J. Li, *Light: Sci. Appl.* **2020**, *9*, 75.
[6] L. C. Wang, W. L. Song, D. Fang, *ACS Appl. Mater. Interfaces* **2019**, *11*, 3450.
[7] Z. Song, C. Lv, M. Liang, V. Sanphuang, K. Wu, B. Chen, Z. Zhao, J. Bai, X. Wang, J. L. Volakis, L. Wang, X. He, Y. Yao, S. Tongay, H. Jiang, *Small* **2016**, *12*, 5401.
[8] J. L. Silverberg, A. A. Evans, L. McLeod, R. C. Hayward, T. Hull, C. D. Santangelo, I. Cohen, *Science* **2014**, *345*, 647.
[9] C. L. Wu, F. C. Li, C. W. Pao, D. J. Srolovitz, *Nano Lett.* **2017**, *17*, 249.
[10] N. S. Rajput, A. Banerjee, H. C. Verma, *Nanotechnology* **2011**, *22*, 485302.
[11] Z. Zhao, J. Wu, X. Mu, H. Chen, H. J. Qi, D. Fang, *Sci. Adv.* **2017**, *3*, e1602326.
[12] Z. Yan, F. Zhang, F. Liu, M. Han, D. Ou, Y. Liu, Q. Lin, X. Guo, H. Fu, Z. Xie, M. Gao, Y. Huang, J. Kim, Y. Qiu, K. Nan, J. Kim, P. Gutruf, H. Luo, A. Zhao, K. C. Hwang, Y. Huang, Y. Zhang, J. A. Rogers, *Sci. Adv.* **2016**, *2*, e1601014.
[13] S. Xu, Z. Yan, K. I. Jang, W. Huang, H. Fu, J. Kim, Z. Wei, M. Flavin, J. McCracken, R. Wang, A. Badea, Y. Liu, D. Xiao, G. Zhou, J. Lee, H. U. Chung, H. Cheng, W. Ren, A. Banks, X. Li, U. Paik, R. G. Nuzzo, Y. Huang, Y. Zhang, J. A. Rogers, *Science* **2015**, *347*, 154.
[14] C. C. Chen, C. T. Hsiao, S. Sun, K. Y. Yang, P. C. Wu, W. T. Chen, Y. H. Tang, Y. F. Chau, E. Plum, G. Y. Guo, N. I. Zheludev, D. P. Tsai, *Opt. Express* **2012**, *20*, 9415.
[15] Z. Tian, B. Xu, B. Hsu, L. Stan, Z. Yang, Y. Mei, *Nano Lett.* **2018**, *18*, 3017.
[16] X. Zhang, L. Medina, H. Cai, V. Aksyuk, H. D. Espinosa, D. Lopez, *Adv. Mater.* **2021**, *33*, 2005275.
[17] C. Py, P. Reverdy, L. Doppler, J. Bico, B. Roman, C. N. Baroud, *Phys. Rev. Lett.* **2007**, *98*, 156103.
[18] N. Bassik, G. M. Stern, D. H. Gracias, *Appl. Phys. Lett.* **2009**, *95*, 091901.
[19] C. Dai, Z. Lin, K. Agarwal, C. Mikhael, A. Aich, K. Gupta, J. H. Cho, *Nano Lett.* **2020**, *20*, 6697.
[20] C. Dai, L. Li, D. Wratkowski, J. H. Cho, *Nano Lett.* **2020**, *20*, 4975.
[21] Z. Liu, H. Du, J. Li, L. Lu, Z. Y. Li, N. X. Fang, *Sci. Adv.* **2018**, *4*, eaat4436.
[22] S. Yang, Z. Liu, H. Yang, A. Jin, S. Zhang, J. Li, C. Gu, *Adv. Opt. Mater.* **2019**, *8*, 1901448.
[23] N. I. Zheludev, E. Plum, *Nat. Nanotechnol.* **2016**, *11*, 16.
[24] C. A. Chen, W. S. Yeh, T. T. Tsai, Y. D. Li, C. F. Chen, *Lab Chip* **2019**, *19*, 598.
[25] A. Benouhiba, L. Wurtz, J. Y. Rauch, J. Agnus, K. Rabenorosoa, C. Clevy, *Adv. Mater.* **2021**, *33*, 2103371.
[26] K. Chalapat, N. Chekurov, H. Jiang, J. Li, B. Parviz, G. S. Paroanu, *Adv. Mater.* **2013**, *25*, 91.
[27] N. S. Rajput, Z. Tong, H. C. Verma, X. Luo, *Micro Nano Lett.* **2015**, *10*, 334.
[28] R. H. Pan, Z. Liu, W. Zhu, C. Z. Gu, J. J. Li, *Adv. Funct. Mater.* **2021**, *31*, 2100689.
[29] S. Du, Z. Liu, H. F. Yang, J. J. Li, C. Z. Gu, *Micro and Nano Eng.* **2020**, *9*, 100076.
[30] Y. Mao, Y. Pan, W. Zhang, R. Zhu, J. Xu, W. Wu, *Nano Lett.* **2016**, *16*, 7025.
[31] O. Y. Rogov, V. V. Artemov, M. V. Gorkunov, A. A. Ezhov, D. N. Khmelenin, *J. Microsc.* **2017**, *268*, 254.
[32] J. H. Cho, M. D. Keung, N. Verellen, L. Lagae, V. V. Moshchalkov, P. Van Dorpe, D. H. Gracias, *Small* **2011**, *7*, 1943.
[33] J. Li, Z. Liu, *Nanophotonics* **2018**, *7*, 1637.
[34] B. Bircan, M. Z. Miskin, R. J. Lang, M. C. Cao, K. J. Dorsey, M. G. Salim, W. Wang, D. A. Muller, P. L. McEuen, I. Cohen, *Nano Lett.* **2020**, *20*, 4850.